

Investigating the Internalization and COVID-19 Antiviral Computational Analysis of Optimized Nanoscale Zinc Oxide

Mohamed Hamdi, Hend Mohamed Abdel-Bar,* Enas Elmowafy, Ahmed El-khouly, Mai Mansour, and Gehanne A.S. Awad

Cite This: <https://dx.doi.org/10.1021/acsomega.0c06046>

Read Online

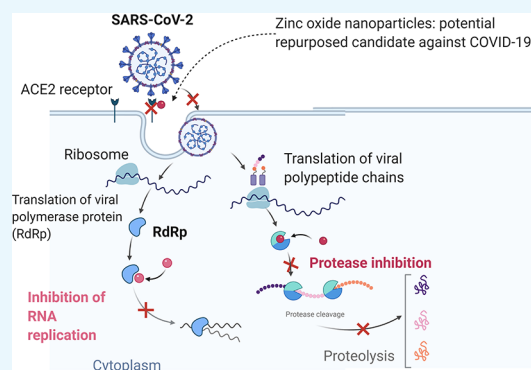
ACCESS |

Metrics & More

Article Recommendations

Supporting Information

ABSTRACT: Global trials are grappling toward identifying prosperous remediation against the ever-emerging and re-emerging pathogenic respiratory viruses. Battling coronavirus, as a model respiratory virus, via repurposing existing therapeutic agents could be a welcome move. Motivated by its well-demonstrated curative use in herpes simplex and influenza viruses, utilization of the nanoscale zinc oxide (ZnO) would be an auspicious approach. In this direction, ZnO nanoparticles (NPs) were fabricated herein and relevant aspects related to the formulation such as optimization, structure, purity, and morphology were elucidated. In silico molecular docking was conducted to speculate the possible interaction between ZnO NPs and COVID-19 targets including the ACE2 receptor, COVID-19 RNA-dependent RNA polymerase, and main protease. The cellular internalization of ZnO NPs using human lung fibroblast cells was also assessed. Optimized hexagonal and spherical ZnO nanostructures of a crystallite size of 11.50 ± 0.71 nm and positive charge were attained. The pure and characteristic hexagonal wurtzite *P63mc* crystal structure was also observed. Interestingly, felicitous binding of ZnO NPs with the three tested COVID-19 targets, via hydrogen bond formation, was detected. Furthermore, an enhanced dose-dependent cellular uptake was demonstrated. The obtained results infer a rationale, awaiting validation from further biological and therapeutic studies.



INTRODUCTION

The ever-emerging and re-emerging respiratory viral infections pose significant threats to public health and sudden devastating consequences. Among the highly pathogenic respiratory viruses SARS, MERS, and COVID-19, three strains of coronaviruses, have been recognized with variable clinical presentations and severity among humans.¹ To deliver their genome into the host cell, SARS-CoV2 are endocytosed prior to fusion with the cell membrane. Viral cellular internalization is triggered by the interaction between the protein viral spike (S) and the angiotensin-converting enzyme 2 (ACE2) receptor.² The proteolysis of the CoV S proteins, important for the induction of cell–cell fusion, occurs by various enzymes including TMPRSS2 (transmembrane serine protease 2) during the first entry inside the infected cell.³ The SARS-CoV2 virus will, then, dismantle to liberate the nucleocapsid and the viral genome. Three carbon-like protease and the papain-like protease, nonstructural protein (3CLpro, nsp5 and PLpro, nsp3) enzymes, are also involved in the splitting of these proteins to yield nsp2–16, essential for replication–transcription complex formation.⁴ In addition, RNA-dependent RNA polymerase (RdRp) is of crucial importance in the SARS-CoV2 life cycle, by mediating the transcription and replication of the viral RNA genome through the infection.⁵

Zinc (Zn) is an indispensable micronutrient in all body tissues, performing an eminent function in the formation of proteins and nucleic acids and neurogenesis. Zn is listed as a safe material by FDA.⁶ In the aspect of antiviral therapy, it presents direct and virus-specific actions, in particular respiratory viruses, and boosts potential antiviral immunity and resistance.⁷ Zn is reported to impede both SARS-COV and retrovirus in vitro RNA polymerase activity, as well as zinc ionophores which hinder the viruses' replication in cell culture.⁸ Zn was also found to inhibit the viral replication of different RNA viruses such as influenza virus, respiratory syncytial virus, and several picornaviruses.^{9,10}

Nanoparticles (NPs) are known to possess superior benefits such as improved potency at low concentrations, augmented efficacy against drug-resistant viruses, cost-effectiveness, and availability for surface modification.¹¹ In an article published in October 2020, the antiviral mechanisms of action for metal NPs

Received: December 11, 2020

Accepted: February 24, 2021

had been well reported.¹² It includes competition at cell-binding sites, prevention of host penetration, inactivation of the virus particles before cellular entry, association with the viral genome, and last but not least the exchange with replication factors. Silver and gold NPs were reported to inhibit viral cell entry and glycoprotein attachment, respectively. Copper metal NPs block the site of viral attachment hindering its entry into target cells, in addition to an activity in demolishing the viral genome and distorting the capsid. Zinc oxide (ZnO) NPs were reported to impede with DNA polymerase activity of the virus leading to hampering of viral replication. Iron NPs preferentially bind to the virus hindering cell binding. Meanwhile, selenium NPs were reported to inhibit cell apoptosis caused by the infection.^{13–15}

ZnO NPs have been exploited against herpes simplex virus type 1¹¹ and H1N1 influenza virus.¹⁶ Comparatively, the well-documented supremacy and better performance of ZnO NPs over other antiviral metal oxide NPs, such as silver and gold NPs, emanate from their good compatibility to biological systems, low price, high safety, and stability.⁶ In addition, its inertness with a wide variety of pharmaceuticals has been reported.¹⁷ Furthermore, stable visible fluorescence of ZnO can be implemented in bioimaging and monitoring the drug delivery and internalization.^{18,19} All the premises of ZnO NPs presented to have the prospect to design nanomedical viral-targeting therapy.

The aim of this study was to adopt various preparation and process parameters to fabricate optimized ZnO NPs, using the Box–Behnken design (BBD). The developed ZnO NPs with minimum crystallite size were subjected to different *in vitro* characterizations and cellular uptakes in human lung fibroblast cells studies. The mechanism of ZnO NPs against COVID-19 targets, namely, the ACE2 receptor, COVID-19 RdRp, and main protease (Mpro) were explored via *in silico* docking studies.

RESULTS AND DISCUSSION

Due to its simplicity and low cost, ZnO NP fabrication by the precipitation method has received great attention. It is a simple, cost-effective technique that does not require a high temperature of reaction or sophisticated equipment.²⁰ In addition, ZnO NP properties are known to depend on both size and morphology of its particles. Nevertheless, particle size was reported to significantly affect the *in vivo* nanoparticle biodistribution, blood circulation time, cellular internalization, and clearance.²¹

ZnO Nanostructure Fabrication. The four main consecutive steps in the chemical precipitation are: (i) hydrolysis of zinc salt to form the intermediate precursor zinc hydroxide (Zn(OH)₂), (ii) nucleation by condensation of monomers to form particles, (iii) growth of particles, and (iv) aging.²² In this technique, zinc nitrate and sodium hydroxide were utilized as a precursor and a precipitator, respectively. Meanwhile, to avoid the formation of nanostructure aggregates, the zinc nitrate solution was admixed with polyvinylpyrrolidone (PVP).²³

Optimization of ZnO NP Size Using BBD. Based on the highest R² and the lowest PRESS values, the quadratic model was nominated as the best fit statistical model for crystallite size response (Table S1).

Effect of Different Critical Process Parameters (CPPs) on Crystallite Size. Table 1 reveals that the fabricated ZnO NPs had crystallite size in a range of 10–62 nm. The influence of the significant CPPs on crystallite size was defined according to the following equation where the nonsignificant variables were omitted:

Table 1. Experimental Design Matrix of the CPPs and the Related Critical Quality Attributes Adopted for the Preparation of ZnO NPs

run	CPPs			critical quality attributes (CQAs)
	A:zinc nitrate concentration (mM)	B:pH	C:speed (rpm)	crystallite size (nm) ^{a,b}
1	300	11	1000	39 ± 3.11
2	300	10	750	24 ± 1.89
3	300	10	750	25 ± 2.87
4	100	11	750	62 ± 5.68
5	500	10	1000	10 ± 0.58
6	300	10	750	26 ± 1.68
7	100	10	1000	41 ± 3.24
8	300	10	750	28 ± 1.27
9	300	10	750	25 ± 1.69
10	500	10	500	23 ± 2.34
11	300	11	500	39 ± 3.11
12	500	9	750	27 ± 1.25
13	500	11	750	17 ± 1.98
14	300	9	1000	25 ± 3.54
15	300	9	500	42 ± 4.74
16	100	9	750	42 ± 2.69
17	100	10	500	54 ± 2.75

^aDetermined from X-ray powder diffraction (XRD) data using Scherrer's equation. ^bResults are expressed as mean ± SD (n = 3).

$$\begin{aligned} \text{Crystallite size} = & +25.60 - 15.25 A + 2.63 B - 5.38 C \\ & - 7.5 AB + 4.25 BC + 3.57 A^2 + 7.82 \\ & B^2 + 2.83 C^2 \end{aligned} \quad (1)$$

The analysis of variance (ANOVA) results are listed in Table S2 where the regression coefficient *p*-values < 0.05 were considered significant. Equation 1 and Figure 1a–c, prove that ZnO NP crystallite size is negatively associated with the increase in Zn nitrate concentration (A) and stirring speed (C). On the contrary, solution pH (B) varied in effects; smaller-sized ZnO NPs were seen at pH 10, while particle size enlargement was obtained at pH 9, which grew significantly at pH 11.

Actually, it was reported that higher zinc precursor concentration (A) causes higher solution supersaturation with the consequent rapid construction of many small-sized nuclei²⁴ which reduces the supersaturation threshold and impedes crystal growth.^{22,25}

Generally, OH[−] ion amounts depend on the solution pH (B) affecting Zn(OH)₂ hydrolysis and ZnO nucleation.^{20,22} A higher alkaline pH would increase the solubility of Zn(OH)₂ which would promote the growth of ZnO NPs.²⁰ Accordingly, a pH of around 10 would produce smaller-sized NPs.

Finally, increasing the stirring speed (C) could impede metal ion nucleation, decreasing NP agglomeration.²⁶ The mechanical shear associated with increasing the stirring speed could also ensure optimum mixing of the stabilizer minimizing the crystallite size.²⁷ Both the negative and positive interactions between AB (Figure 1d) and BC (Figure 1e), respectively, delineated the importance of pH and speed control for the prevalence to obtain small-sized crystals of ZnO at the highest precursor concentration.²²

Design Space and Optimization. Figure S1 illustrates the optimum CPP values to achieve the quality target product profile (QTTP) criteria, minimum crystallite size (expressed as a yellow area). Based on the highest desirability (0.974), one

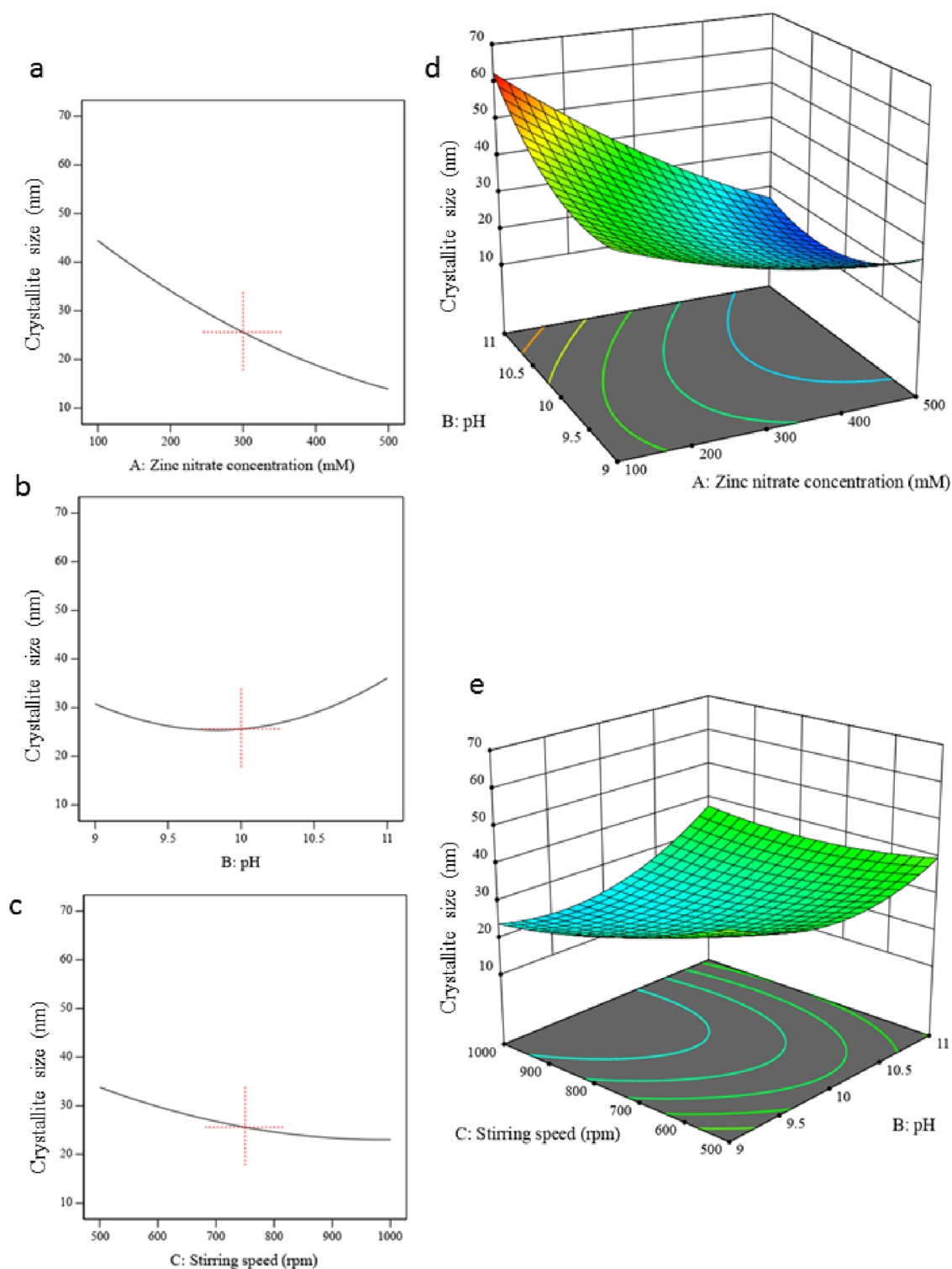


Figure 1. Response 1D and 3D plots of the main effect (a–c) of different significant CPPs and their interactions (d and e) on ZnO NP crystallite size. Figures a and c show small nuclei formation at higher zinc nitrate concentration (A) and stirring speed (C). The pH (B) with its enhancement effect on $\text{Zn}(\text{OH})_2$ hydrolysis and nucleation affected variably the NP sizes: smaller NPs were obtained at pH 10 with higher values at extreme limits especially at pH 11. AB and BC had contradicting interaction effects where AB decreased the crystallite size (d) and BC increased it (e) indicating that a combination of the three factors should be adjusted together to obtain the smaller ZnO crystals.

formula was selected and prepared as a checkpoint. Table 2 illustrates its composition and predicted and experimental crystallite size. The small values of the % predicted error verified the suitability of the developed models to optimize the fabrication of ZnO NPs.

In Vitro Characterization of the Optimized ZnO NPs. X-ray Powder Diffraction (XRD). Figure 2a demonstrates the diffractogram of the optimized ZnO NPs with characteristic peaks at 2θ of 31.73, 34.42, 36.23, 47.51, 56.53, 62.83, 67.89, and 69.02° identical to the hexagonal wurtzite $P63mc$ crystal

Table 2. Experimental and Predicted Crystallite Size of the Optimized ZnO NPs

formula	zinc nitrate molar concentration (mM)	pH	stirring speed (rpm)	crystallite size (nm)		
				exp. ^{a,b}	pre.	% pre. error
ZnO NPs	500	10	1000	11.50 ± 0.71	11.34	1.42

^aDetermined from XRD data using Scherrer's equation. ^bResults are expressed as mean ± SD (n = 3).

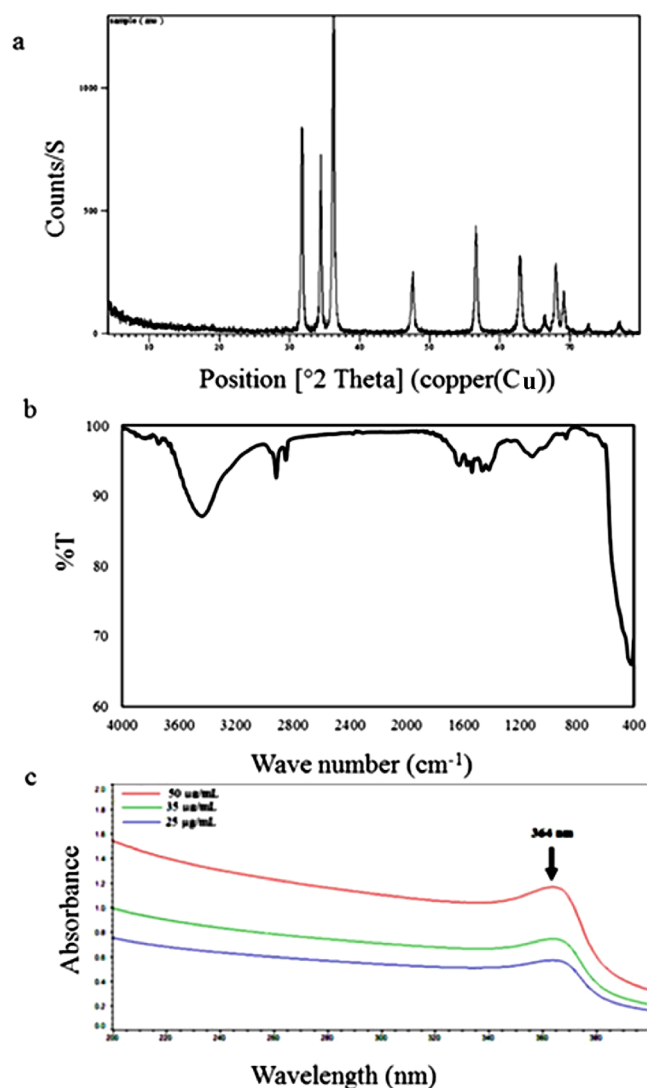


Figure 2. (a–c) Characterization of the optimized ZnO NPs with XRD, FT-IR, and UV spectroscopy. The XRD pattern of the optimized ZnO NPs depicts the characteristic peaks of the hexagonal wurtzite *P63mc* crystal structure (a). The FT-IR spectrum of the optimized ZnO NPs revealed an obvious peak at 430 cm^{-1} assigned to Zn–O stretching (b). The UV spectrum of different concentrations of ZnO NPs in deionized water showed a characteristic peak at 364 nm of ZnO (c).

structure. These results indicate the successful fabrication of ZnO NPs.^{28–30} The experimental crystallite size of the optimized ZnO NPs was 11.50 ± 0.71 nm (Table 2).

ZnO Nanostructure Elucidation. *Fourier Transform Infrared (FT-IR) Spectroscopy.* Figure 2b shows the FT-IR spectrum of the optimized ZnO NPs where the characteristic ZnO NP absorption bands could be observed at 3400 and 430

cm^{-1} assigned to O–H and Zn–O stretching, respectively, confirming the formation of ZnO NPs.^{31,32} The bands at 1650, 1430, and 1265 cm^{-1} resulted from stretching vibration of C=O, the attached CH_2 groups, and C–N in the pyrrole ring of PVP, respectively.³¹

UV Spectroscopy. The spectral scanning of serial concentrations of the optimized ZnO NPs in deionized water revealed a maximum absorbance (λ_{max}) at 364 nm corresponding to the pure ZnO confirming the successful fabrication of the NPs (Figure 2c).³³

Morphological Studies. Figure 3a shows the scanning electron microscopy (SEM) micrograph of the ZnO NP surface which appeared as radial hexagonal, rectangle, and spherical NPs in crystallite size ranging from 10 to 15 nm. The compositional analysis of ZnO NPs was ascertained by energy-dispersive X-ray spectroscopy (EDX) analysis (Figure 3b). The weight % of Zn and O elements were 77.57 and 22.43%, respectively.²⁰ The absence of any additional peaks indicates the purity of the obtained ZnO NPs. Transmission electron microscopy (TEM) evidenced the formation of hexagonal and spherical structures with crystallite size < 20 nm (Figure 3c). The atomic force microscopy (AFM) micrograph shows the 3D structure of the optimized ZnO NPs (Figure 3d) with a homogeneous and smooth surface of the NPs confirmed by a roughness value of 1.29. The measured sizes by AFM, SEM, TEM, and by applying Scherrer's equation on the data derived from the XRD study were all consistent.

Zeta Potential. The assessment of surface charge of NPs is critical as it will distinctly affect their interaction with the biological membranes. Over the studied pH range, a sequential charge reversal on the surface of ZnO NPs was manifested from positive to neutral and thereafter to negative. The measured zeta potential values of the optimized ZnO NPs were in the range from +25.32 ± 3.21 to –18.78 ± 1.58, highly dependent on the dispersant medium pH (Figure 4a). At physiological pH, the measured zeta potential value of ZnO NPs was +9.32 ± 1.89 mV which is in line with earlier results.³⁴ The domain of the positive charge of the obtained ZnO NPs below pH 8 could be attributed to the fact that the ZnO NP isoelectric point is at pH 8.2.³⁵

In Vitro Zn^{2+} Release. The release profiles of Zn^{2+} from the optimized ZnO NPs at pH 5.5 and 7.4 are displayed in Figure 4b where a pH-dependent release was seen which is consistent with previous reports.^{36,37} The higher Zn^{2+} solubility in the acidic medium is the reason for the higher Zn release at pH 5.5.³⁸ However, only 11.17 ± 1.9% of Zn^{2+} was released after 48 h in pH 7.4 in the presence of serum. This controlled release pattern would avoid drug leakage in systemic circulation.³⁹

Molecular Docking. Different compounds that could interact with different SARS-CoV2 targets are assumed to impede viral attachment to host receptors and subsequently hamper the viral infection process.⁴⁰ In this context and due to the efficiency of ZnO NPs in various respiratory infections, the mechanism of the possible interaction between ZnO NPs and the assigned COVID-19 target portions could be investigated.⁴¹ The hexagonal wurtzite structure of ZnO NPs was constructed using the crystallographic parameters derived from XRD. The hexagonal crystal system consisted of the *P63mc* space group, a (\AA) = b (\AA) = 3.2530, c (\AA) = 5.2070, α ($^\circ$) = β ($^\circ$) = 90.00, and γ ($^\circ$) = 120.00. The structure parameters: For (Zn) x = 0.33333, y = 0.66666, z = 0.0000, Biso = 0.8000 and sof = 0.9980 and for (O) x = 0.33333, y = 0.66666, z = 0.38260, Biso = 0.9000 and sof = 1.0000. In addition, for COVID-19 RdRp: Ligands were centered with a spacing of 1.0 \AA , size X = 15, size Y = 15, size Z =

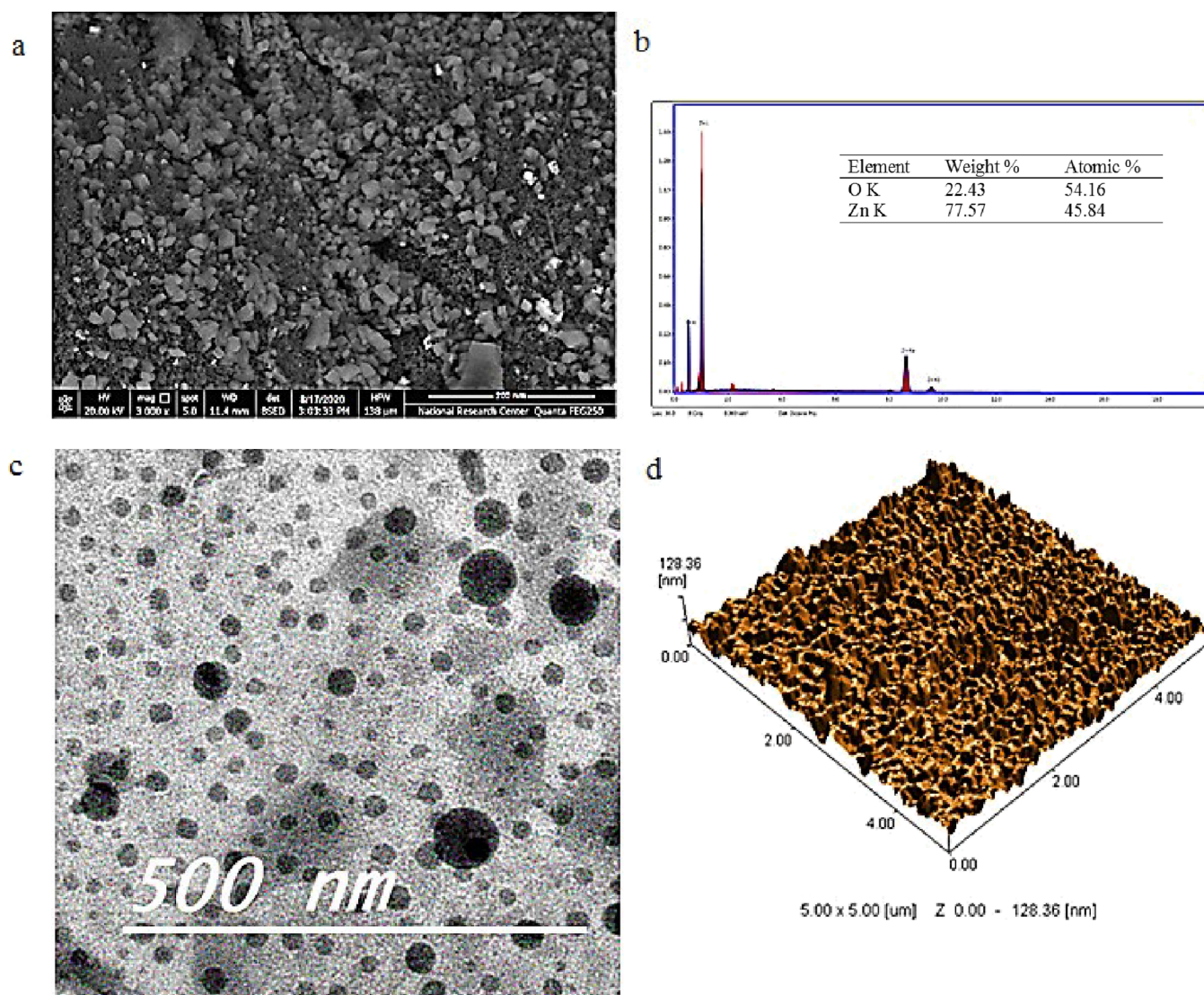


Figure 3. Morphological characterization of the optimized ZnO NPs. SEM micrograph (a), EDX (b), TEM micrograph (c), and AFM micrograph 3D view (d). ZnO NPs appeared as hexagonal and round nanostructures with crystallite size values consistent with the XRD technique.

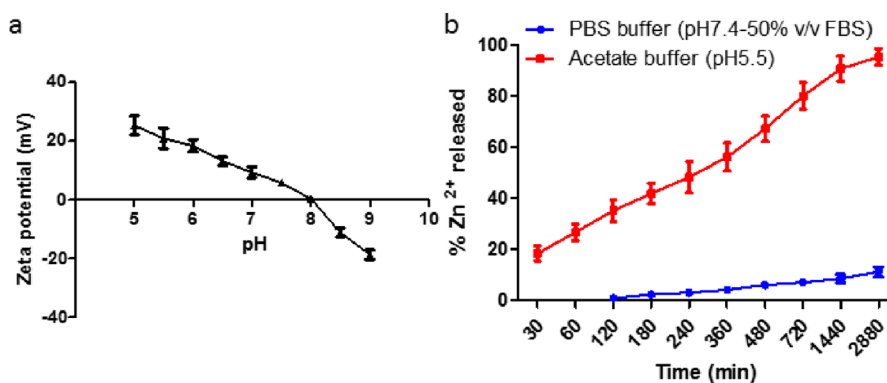


Figure 4. In vitro characterization of the optimized ZnO NPs. Zeta potential measurement at pH 5–9 measured by dynamic light scattering technique (a). The optimized ZnO NPs showed that the positive–negative surface charge reversal is dependent on pH ($n = 3$). In vitro release profile of Zn²⁺ from the optimized ZnO NPs in phosphate buffered saline (PBS) (pH 7.4) in the presence of fetal bovine serum (FBS) (50% v/v), or in acetate buffer (pH 5.5) at 37 °C (b). Zn²⁺ release from ZnO NPs was measured by suspending ZnO NPs in either PBS (pH 7.4) in the presence of 50% FBS or acetate buffer (pH 5.5). At each time interval, the release medium was collected and centrifuged using ultrafiltration (MW CO 3.5 K at 14,000 rpm, 45 min). The obtained filtrate was mixed with concentrated nitric acid (0.5 mL). The amount of dissolved Zn²⁺ was quantified by inductively coupled plasma-atomic emission spectroscopy. Datapoint represents mean and SD ($n = 3$).

Table 3. Docking Interaction Parameters of the Optimized ZnO NPs with Different SARS-CoV2 Targets

target	ligand	binding free energy (kcal/mol)	targeted amino acid ^{a,b}	total hydrogen bond number	π - π interactions	π -cation interactions	Ki (μ M)
ACE2	ZnO NPs	-5.7	Thr282, Lys511, His513	3	0	0	64.072
	captopril (positive control)	-6.5	His383 (2), His353, His513	4	0	0	16.525
COVID-19 RdRp	ZnO NPs	-5.4	Arg555, Ser759, u10, u20	4	0	0	106.51
	remdesivir (positive control)	-8.0	Arg555, Asn691, u10, u20 (4)	7	0	1	1.302
COVID-19 Mpro	ZnO NPs	-4.5	Cys145, Glu166, His163	3	0	0	489.19
	saquinavir (positive control)	-7.3	His163 Leu141Ser144 (2) Asn124	5	0	0	4.2618

^aThr: threonine, Lys: lysine, His: histidine, Arg: arginine, Ser: serine, u: uracil, Asn: asparagine, Cys: cysteine, Glu: glutamic acid, Leu: leucine.
^bThe commonly targeted amino acids for both ZnO NPs and the respective positive controls are denoted in bold.

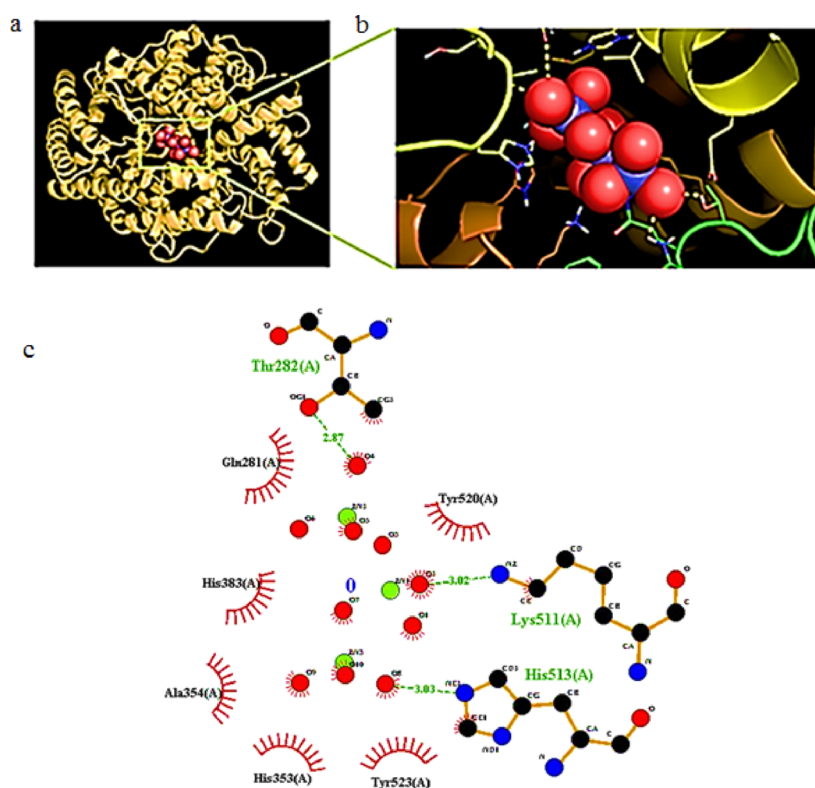


Figure 5. Docked poses of the optimized ZnO NPs with ACE2 (PDB ID: 1UZF). The Pymol 3D schematic diagram of the interaction of ZnO NPs and surrounding amino acids of ACE2 active sites (a) and magnified view (b). The LigPlot+2D view of the interaction of ZnO NPs with the surrounding amino acids of ACE2 (c). Hydrogen bonds are indicated by dashed green lines between the atoms involved.

15 and center X = 94.265, center y = 91.142 and center z = 104.101. For COVID-19 Mpro: Ligands centered with a spacing of 1.0 Å, size X = 15, size Y = 12, size Z = 15 and center X = -8.433, center y = -0.232 and center z = 20.977. For the ACE2 receptor: Ligands centered with a spacing of 1.0 Å, size X = 10, size Y = 10, size Z = 12 and center X = 41.440, center y = 34.709 and center z = 20.977.

The docking protocol was validated by redocking the same conformer of the cocrystallized ligand with root mean square deviation (RMSD) = 1.021 for COVID Mpro in which the cocrystallized ligand was 2-(5-cyanopyridin-3-yl)-N-(pyridine-3-yl) acetamide and with RMSD = 0.43 for ACE in which the cocrystallized ligand was captopril (Figure S2). This step could not be applied for COVID-19 RdRp because the cocrystallized remdesivir ligand was broken in the protein crystal, i.e., could not be aligned with the redocked one.

Table 3 demonstrates the recorded binding affinity values of ZnO NPs and the three tested SARS-CoV2 targets of the chosen model virus. The association of the optimized ZnO NPs possesses a binding energy of -5.7, -5.4, and -4.5 kcal/mol for ACE2, COVID-19 RdRp, and COVID-19 Mpro, respectively. Accordingly, the binding affinity of ZnO NPs could be ranked in the following descending order as ACE2 > COVID-19 RdRp > COVID-19 Mpro. The binding energy's negative charge for the interaction between the optimized ZnO NPs and the three assigned targets reveals the possible association between ZnO NPs and the tested proteins.⁴²

Figure 5 shows that the optimized ZnO NPs are involved in hydrogen bond formation with Thr282, Lys511, and His513 amino acids in the ACE2 receptor. Interestingly, captopril, the positive control with binding energy -6.5, was also able to form three hydrogen bonds with ACE2 receptors at His383 (2), His353, and His513 (Table 3 and Figure S3). Neither ZnO NPs

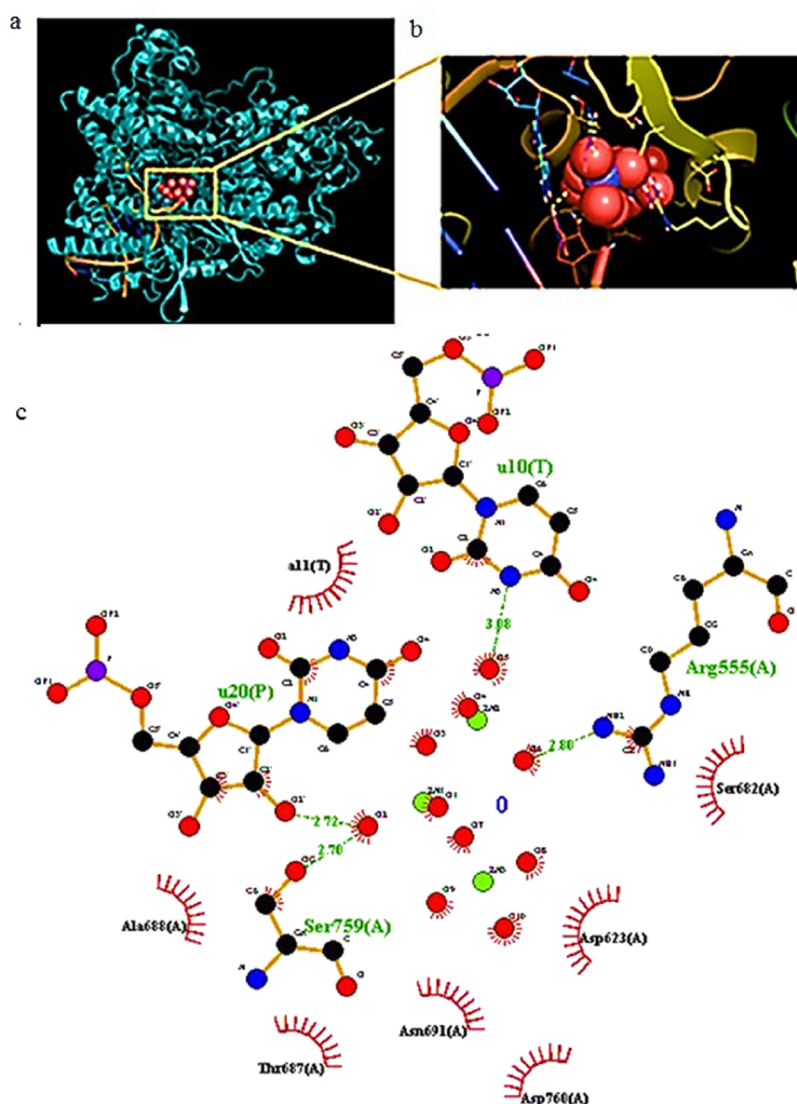


Figure 6. Docked poses of the optimized ZnO NPs with COVID-19 RdRp (PDB ID: 7BV2). The Pymol 3D schematic diagram of the interaction of ZnO NPs and surrounding amino acids of COVID-19 RdRp active sites (a) and magnified view (b). The LigPlot⁺ 2D view of the interaction of ZnO NPs with the surrounding amino acids of COVID-19 RdRp (c). Hydrogen bonds are indicated by dashed green lines between the atoms involved.

nor captopril was involved in π - π interactions or π -cation interactions with respective inhibition constant (K_i) 64.072 and 16.525 μM (Table 3). In addition, the interaction of ZnO NPs and COVID-19 RdRp was elucidated to be via hydrogen bond formation with Arg555 and Ser759 amino acids. Moreover, ZnO NPs were capable of forming the other two hydrogen bonds with u10 and u20 uracil bases of the protein crystal in the same manner that remdesivir binds to RdRp (Table 3 and Figure S4) but with a fewer number of hydrogen bonds (Figure 6). The calculated K_i values of ZnO NPs and remdesivir were 106.51 and 1.302 μM , respectively. The expected superior activity of remdesivir could be also attributed to its ability to form π -cation interaction.

Finally, docking results revealed that ZnO NPs could interact with the virus Mpro via hydrogen bonding and also at Cys145, Glu166, and His163 amino acids in the protein (Figure 7). By inspecting the docking data of saquinavir, the positive control for COVID-19 Mpro, it could be deduced that it also interacts with the assigned target with hydrogen bonds (Table 3 and Figure S5). The calculated K_i values were 489.19 and 4.2618 μM for ZnO NPs and saquinavir, respectively. Interestingly, the

hydrogen bond has an essential role in stabilizing the interaction of ligands with protein active sites.^{43,44} However, there are several concerns about the predicted K_i that could result in poor correlation with the experimental K_i as the role of solvent, the inadequate description of H-bonding, and the absence of the systems' true dynamics.⁴⁵

The obtained *in silico* docking results correlated well with the reported role of Zn in antiviral immune response.¹⁰ The antiviral Zn efficiency against different viruses is reported via inhibiting host-virus attachment, polymerase and protease enzymes.⁴⁶ A previous study reported the positive effect of Zn on rat bronchial cilia numbers and the length that advanced the viral removal from lung tissue and prevented the secondary acquired bacterial infection.⁴⁷ Zn, also, has a vital role in improving lung integrity in murine models *in vivo* attributed to the Zn-dependent nature of tight junction proteins as Claudin-1 and ZO-1.^{48,49} The stabilization of protein structures which affects the substrate affinity to many metalloproteins as ACE2 is enhanced by Zn.^{50,51} The inhibitory effect of Zn on SARS-CoV RdRp occurs by affecting the template binding during the RNA synthesis elongation phase.⁸ In addition, Zn obstructs the viral

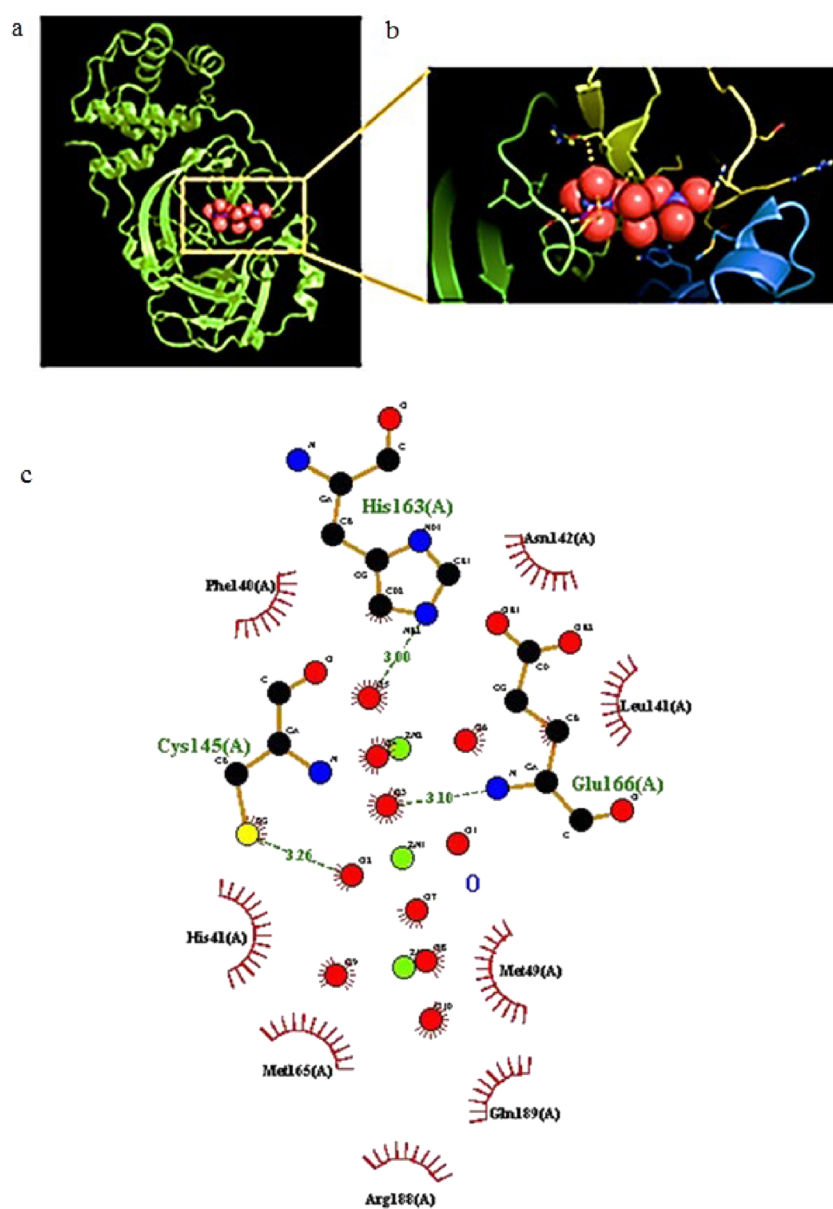


Figure 7. Docked poses of the optimized ZnO NPs with COVID-19 Mpro (PDB ID: SRGW). The Pymol 3D schematic diagram of the interaction of ZnO NPs and surrounding amino acids of COVID-19 Mpro active sites (a) and magnified view (b). The LigPlot+ 2D view of the interaction of ZnO NPs with the surrounding amino acids of COVID-19 Mpro (c). Hydrogen bonds are indicated by dashed green lines between the atoms involved.

polyprotein proteolytic process by the misfolding viral protease enzyme in picorna virus, coronavirus, encephalomyocarditis virus, and poliovirus.^{9,52} Moreover, Zn could bind to the histidine residue viral E1 protein that could inhibit membrane fusion of many viruses like respiratory syncytial virus, herpes simplex virus, Semliki Forest virus, and sindbis viruses.⁵³

Hemolytic Activity of ZnO NPs. The effect of nanomaterials on red blood cells (RBCs) is considered one of the simplest and consistent techniques for assessing their hemocompatibility.⁵⁴ Figure 8 shows that ZnO NPs had a dose-dependent increase in hemolytic activity ($p < 0.05$). Nevertheless, all the tested concentrations showed % hemolysis less than 5% which is considered acceptable according to the new consensus ASTM E2524-08—a standard test method for analysis of hemolytic properties of nanoparticles.⁵⁵

Cellular Uptake of ZnO NPs. High cell viability exceeding 90% was obtained up to a concentration of 80 $\mu\text{g}/\text{mL}$ ZnO NPs

(Figure S6). A significant reduction in cell viability could be depicted at 100 $\mu\text{g}/\text{mL}$ concentration of ZnO NPs ($p < 0.05$). This could be attributed to the ability of the induction of reactive oxygen species.⁵⁶

The interaction of NPs with cells and subsequent endocytic intracellular concentration is important for boosted delivery and efficacy. Flow cytometry is a cost-effective, rapid, and easy method to perform quantification of targeting ability and cellular internalization efficiency of NPs with robust statistics.⁵⁷ The right shift in the cell-associated fluorescence signal following incubation of NPs with cells indicates an increase in its intensity and hence high intracellular NP concentration. Exploiting the inherent photoluminescence intensity of ZnO NPs in optical imaging applications is well documented in earlier studies.⁵⁸

The cellular uptake of the optimized ZnO NPs into CCD-19Lu cells was studied by flow cytometry depending on its intrinsic fluorescence properties.⁶ Figure 9a demonstrates a

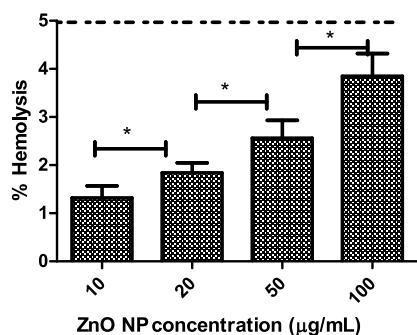


Figure 8. In vitro hemolysis assay of ZnO NPs. Rat RBCs were incubated with the optimized ZnO NPs at different concentrations (10–100 µg/mL) for 2 h at 37 °C. Positive and negative controls were 0.5 w/v% Triton X-100 and PBS (pH 7.4), respectively. Samples were centrifuged at 4000 rpm for 5 min at 4 °C and the absorbance of the released hemoglobin was determined at 545 nm. Results are expressed as mean \pm SD ($n = 3$). The dotted line represents the acceptable hemolysis range.

representative histogram of ZnO NP cellular uptake. Furthermore, the cellular uptake extent was quantified as mean fluorescence intensity (MFI).⁵⁹ The optimized ZnO NPs could be efficiently internalized within CCD-19Lu cells as demonstrated by a significant increase in the MFI of cells treated with either 40 or 80 µg/mL in comparison with control cells ($p < 0.05$). A significant ≈ 3 -fold increase of MFI was observed by increasing the concentration of ZnO NPs from 40 to 80 µg/mL ($p < 0.05$) (Figure 9b). A similar concentration-dependent uptake was previously observed.^{60,61}

CONCLUSIONS

Based on their great premises, ZnO NPs were successfully synthesized with a high degree of purity and crystallinity by tuning zinc precursor concentration, reaction pH, and stirring speed. The optimized ZnO NPs had a crystallite size of 11.50 ± 0.71 nm with an identical hexagonal wurtzite *P63mc* crystal structure. From the in silico molecular docking perspective, the possible interaction between ZnO NPs and the ACE2 receptor as a COVID-19 target could occur. In parallel, a dose-dependent cellular uptake of ZnO NPs was attained in CCD-19Lu human

lung fibroblasts. The obtained results suggest the promising competence of the described ZnO NPs for respiratory tract infection outbreaks, posing them either as a standalone option or as combinatory with other pharmacologically effective frontiers for futuristic experimentation and technology transfer.

EXPERIMENTAL SECTION

Materials. Zinc nitrate hexahydrate, sodium hydroxide, polyvinylpyrrolidone, and nitric acid were obtained from Sigma-Aldrich, UK. Gibco minimal essential medium (MEM), FBS, penicillin/streptomycin, trypsin/EDTA, and PBS were obtained from ThermoFisher Scientific (UK).

Methods. Zinc Oxide Nanostructures Fabrication. Different ZnO NPs were prepared using the chemical precipitation method with a slight modification.⁶² Briefly, sodium hydroxide (1 M) solution, to adjust the alkaline pH of the reaction media, was slowly dripped on the wall of a beaker containing 100 mL of aqueous solutions of different concentrations of zinc nitrate hexahydrate and a fixed concentration of 0.1%w/v PVP. The stirring was continued for 4 h at 50 °C. The resultant suspension was centrifuged at 14,000 rpm for 15 min. The collected fine pellets were consecutively washed with deionized water (3X) followed by ethanol (3X). Afterward, the harvested fine powder was dried at 50 °C.

Experimental Design and Construction of Box–Behnken Design. Three-factors, each at the three-level BBD using Design Expert software (Version 12, Stat-Ease Inc. Minneapolis, MN, USA) were applied. The influence of three CPPs; zinc nitrate concentration (A), reaction pH (B), and stirring speed (C) on the crystallite size as the critical quality attribute (CQA) were investigated. The ZnO NPs were fabricated to deliver a QTPP of minimum crystallite size as shown in Table 4. The assigned 17 formulae composition are listed in Table 1. The generated polynomial equation was statistically validated by ANOVA. The crystallite sizes were instantaneously fitted to linear; two-factor interactions (2FI) and quadratic models. The optimized formula with the QTPP was picked based on the highest desirability. One optimum checkpoint was elected to validate the evolved statistical model and equation by comparing the experimental to the predicted crystallite size before further studies.

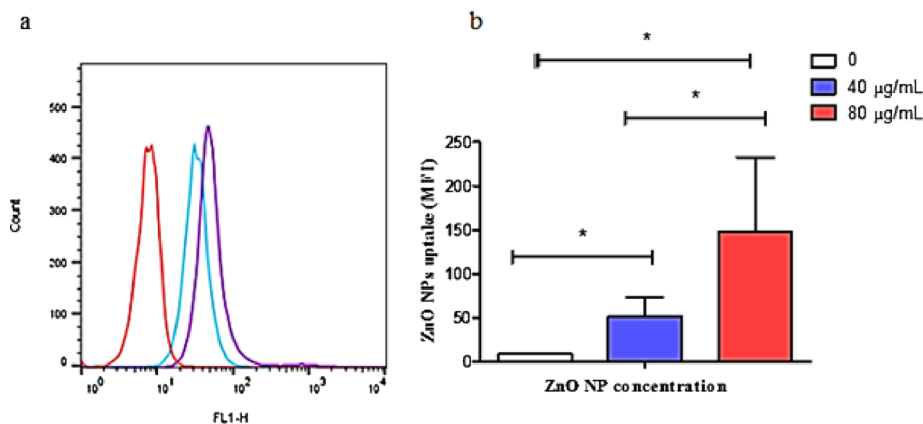
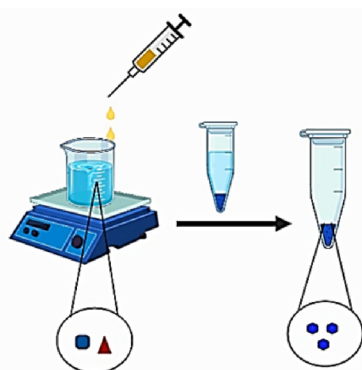


Figure 9. Intracellular uptake of the optimized ZnO NPs in CCD-19Lu human lung fibroblasts by flow cytometry. The flow cytometry histogram for uptake of ZnO NPs in 40 (light blue) or 80 µg/mL (violet) concentrations after 4 h in comparison to the control group (red) (a). Cellular uptake was quantified by MFI using flow cytometry and FL-1 detectors (b). ZnO NP uptake was dose-dependent as observed by a significant increase in MFI by increasing the ZnO NP concentration. Statistical analysis was carried out using one-way ANOVA followed by Tukey post test $*p < 0.05$. Results are expressed as mean \pm SD ($n = 3$).

Scheme 1. ZnO NP Preparation^a

■ Zinc nitrate ▲ Polyvinylpyrrolidone ◆ Sodium hydroxide ● Zinc oxide nanoparticles

^aZnO NPs were prepared by titrating (100 mL) of an aqueous solution of zinc nitrate hexahydrate containing 0.1%w/v of PVP, with 1 M sodium hydroxide on a magnetic stirrer for 4 h at 50 °C. The fabricated ZnO NPs were obtained by centrifugation at 14,000 rpm for 15 min. The collected pellets were washed by deionized water (3X) and ethanol (3X). The washed NPs were dried at 50 °C. Created with [BioRender.com](https://www.biorender.com)

Table 4. Levels of CPPs, Quality Attributes, and QTPPs Used in the Preparation of ZnO NPs Adopting the BBD

CPPs (coded independent variables)	levels		
	low (-1)	medium (0)	high (1)
A: zinc nitrate concentration (mM)	100	300	500
B: reaction pH	9	10	11
C: stirring speed (rpm)	500	750	1000
CQAs (responses)	QTPP (constrains)		
Y1: crystallite size (nm)	minimize		

X-ray Diffraction Analysis of Zinc Oxide Nanoparticles.

Crystal size and different crystallographic parameters were determined using XRD (Philips X'Pert system, The Netherlands). The analysis was conducted with Cu K α radiation in a 2 θ range of 10–80° at 40 kV and 30 mA.²⁸ Crystal size (d) was estimated using Scherrer's equation as follows

$$d = \frac{K\lambda}{\beta \cos\theta} \quad (2)$$

Where K is a dimensionless shape factor = 0.9, λ = 0.15406 nm, β is the line broadening at half the maximum intensity (FWHM), and θ is the Bragg's diffraction angle.²⁸

ZnO Nanostructure Elucidation. FT-IR Spectroscopy. The infrared spectra of the optimized ZnO NPs were recorded on an FT-IR spectrometer (JASCO 4000, USA). A well-mixed mixture of ZnO NPs and KBr (2 mg sample in 100 mg of KBr) was made in a disk and the spectra were recorded in the range of 4000–400 cm⁻¹.⁶³

UV-visible Spectroscopy. Serial concentrations of the optimized ZnO NPs in deionized water were scanned spectrophotometrically within a range of 200–400 nm using the same solvent as blank using a UV-visible double beam spectrophotometer (Evolution 201, Thermo Scientific, UK).

Morphological Studies. Scanning eElectron Microscopy–Energy-Dispersive X-ray Spectroscopy (SEM–EDX). The morphological architecture and chemical composition of the

optimized ZnO NPs were studied using SEM (JXA-840A, Japan) equipped with an EDX unit.

Transmission Electron Microscopy. The optimized ZnO NP suspension in deionized water was deposited on a copper 300-mesh grid, coated with carbon, and allowed to stand for 10 min, then any excess fluid was absorbed by a filter paper. The sample was stained with one drop of 1% phosphotungstic acid and dried for 5 min, then imaged with TEM (Jeol, JEM-1230, Japan).

Atomic Force Microscopy. The 3D surface and topographical profile of the optimized ZnO NPs were investigated by a atomic force microscope (Wet-SPM 9600, scanning probe microscope, Shimadzu, Japan) as described elsewhere. The AFM images were analyzed using noncontact mode software.³³

Determination of Zeta Potential. The optimized ZnO formula was diluted with deionized water (1:10) and the surface charge as zeta potential was measured using Nanosizer ZS Series (Malvern Instruments, UK). The change in the zeta potential of the optimized formula as a function of pH was assessed.

In Vitro Release of Zn²⁺ from ZnO NPs. An accurately weighed amount of ZnO NPs (5 mg) was suspended in a well-closed container filled with 50 mL either PBS pH 7.4 mixed with 50% FBS or acetate buffer pH 5.5 in a thermostatically controlled shaking water bath at 250 strokes/min \pm 0.1 at 37 \pm 0.5 °C. In order to avoid any loss in the ZnO NPs, separate sets of release experiments were assigned for each time point (n = 3). At each time interval, the release medium was collected and centrifuged using ultrafiltration (MW CO 3.5 K at 14,000 rpm, 45 min). The obtained filtrate was mixed with concentrated nitric acid (0.5 mL).⁶⁴ The amount of dissolved Zn²⁺ was quantified by inductively coupled plasma-atomic emission spectroscopy (ICP-AES Prodigy, eledyne Instruments Leeman Labs, USA).

Molecular Docking. The possible binding interaction between the optimized ZnO NPs and the three main targets COVID-19 RdRp, Mpro enzymes, and ACE2 was explored by docking using AutoDock Tools (ADT, Version 1.5.6) available from Scripps Research Institute (<http://autodock.scripps.edu/resources/adt>). Briefly, the 3D crystal structures for COVID-19 different targets were retrieved from protein data bank (PDB) (<https://www.rcsb.org>). The different protein structures were prepared by removing ligand water molecules and heteroatoms. In addition, polar hydrogens and Kollman charges were added and Gasteiger charges were calculated.⁶⁵ Subsequently, the enzymes were converted to PDBQT using AutoDock Tools. The optimized ZnO NP crystal structure as a ligand was generated by VESTA 3 software to visualize the 3D crystal morphology by applying the XRD-derived data.⁶⁶ The generated crystal structure was saved as a protein data bank (pdb) file and then their torsions were set and converted to PDBQT using AutoDock Tools to be suitable for docking studies. Captopril, remdesivir, and saquinavir were selected as a positive controls against ACE2, COVID-19 RdRp, and COVID-19 Mpro, respectively. The 2D schematic diagrams of protein–ligand interactions were generated by LigPlot⁺ software available from <https://www.ebi.ac.uk/thornton-srv/software/LIGPLOT/>.⁶⁵ All the 3D protein–ligand complex visualization was constructed and analyzed using the AutoDock Tools program and the PyMOL molecular graphics program (www.pymol.org).⁶⁷ The K_i values for ZnO NPs and positive controls were calculated from the binding free energy according to the following equation⁶⁸

$$\exp\left(\frac{\Delta G \times 1000}{R \times T}\right) \quad (3)$$

where ΔG is the binding energy, R is the gas constant, and T is the absolute temperature.

Hemolysis Test. The hemolytic activity of ZnO NPs was evaluated using fresh male albino rat's RBCs.⁵⁹ The experimental procedures conformed to the Ethics Committee, of the Faculty of Pharmacy, Ain Shams University on the use of animals. Briefly, 1 mL blood was withdrawn by cardiac puncture into a heparinized tube and the blood was centrifuged at 4000 rpm for 10 min. The obtained RBCs were incubated with serial concentrations of ZnO NPs (10–100 $\mu\text{g}/\text{mL}$) in PBS pH 7.4 for 2 h at 37 °C. All samples were then centrifuged for 5 min at 4000 rpm and 4 °C. The absorbance of the obtained supernatant was determined at 545 nm. Fresh RBCs incubated with 0.5% v/v Triton X-100 or PBS pH 7.4 were used as a positive and negative control, respectively. The % hemolysis was calculated using the following equation:

$$\% \text{ hemolysis} = \frac{\text{absorbance sample} - \text{absorbance negative control}}{\text{absorbance positive control} - \text{absorbance negative control}} \times 100 \quad (4)$$

In Vitro Cellular Uptake of Zinc Oxide Nanoparticles.

In Vitro MTT Cytotoxicity Assay. Human lung fibroblast (CCD-19Lu) cells were cultured in MEM media supplemented with 10% v/v FBS, 50 U/mL penicillin, 50 $\mu\text{g}/\text{mL}$ streptomycin, and 1% v/v L-glutamine and seeded in a 96-well plate at a density of 10 K/ well for 24 h. Subsequently, cells were incubated with serial concentrations of the optimized ZnO NPs in a range of 10–100 $\mu\text{g}/\text{mL}$ for 24 h. The media were then removed and the cells incubated with MTT solution (120 μL) at 37 °C and 5% CO₂ for 4 h. Consequently, DMSO (200 μL) was added to dissolve the formed formazan crystals. The plate was read at 570 nm using a FLUO star OPTIMA plate reader (BMG Labtech).⁶⁹ The results were expressed as the percentage cell survival and calculated using the following equation:

$$\% \text{ cell survival} = \frac{\text{A570 nm of treated cells}}{\text{A570 nm of untreated control cells}} \times 100 \quad (5)$$

Quantitative Determination of Cellular Uptake by Flow Cytometry. The cellular uptake of the optimized ZnO NPs was assessed using flow cytometry (BD FACS Calibur flow cytometer, BD Biosciences). Human lung fibroblast (CCD-19Lu) cells (catalogue number ATCC CCL-210) were cultured in MEM media supplemented with 10% v/v FBS, 50 U/mL penicillin, 50 $\mu\text{g}/\text{mL}$ streptomycin, and 1% v/v L-glutamine at a density of 50 K cells/well into a 24-well plate for 24 h. Cells were incubated with the optimized ZnO NPs (40 and 80 $\mu\text{g}/\text{mL}$) for 4 h in 5% CO₂ at 37 °C.⁷⁰ Subsequently, cells were washed two times with PBS, trypsinized, and centrifuged at 1750 rpm at 4 °C for 3 min. The harvested cells were resuspended into PBS (pH 7.4, 200 μL). The uptake study was performed at 10 K gated cells by computing the fluorescence using an FL-1 detector, and the obtained data were analyzed using FlowJo software.

Statistical Analysis. All experiments were conducted in triplicate and the results are the mean \pm SD. All statistical analyses were performed using SPSS 18 (Chicago, USA) and differences were considered significant at probability (p) value < 0.05. Two variables were compared by Student's t -test while the

difference between groups was compared by one-way ANOVA followed by Tukey HSD test.

■ ASSOCIATED CONTENT

Supporting Information

The Supporting Information is available free of charge at <https://pubs.acs.org/doi/10.1021/acsomega.0c06046>.

Model summary statistics for crystallite size (Table S1); ANOVA of the obtained data from BBD for the crystallite size of ZnO NPs and associated p -values (Table S2); overlay plots depicting the design space region for the optimized ZnO NPs (Figure S1); Pymol alignment of the recrystallized ligand conformer and the redocked best conformers for the ACE2 receptor and COVID-19 Mpro (Figure S2); docked poses of captopril with ACE2 (PDB ID: 1UZP) (Figure S3); docked poses of remdesivir with COVID-19 RdRp (PDB ID: 7BV2) (Figure S4); docked poses of saquinavir with COVID-19 Mpro (PDB ID: 5RGW) (Figure S5); and cell viability assay of ZnO NPs after incubation for 24 h (Figure S6) (PDF)

■ AUTHOR INFORMATION

Corresponding Author

Hend Mohamed Abdel-Bar – Department of Pharmaceutics, Faculty of Pharmacy, University of Sadat City, Sadat City, Egypt; orcid.org/0000-0001-5833-9267; Email: hend.abdelbar@fop.usc.edu.eg

Authors

Mohamed Hamdi – Department of Pharmaceutics, Faculty of Pharmacy, University of Sadat City, Sadat City, Egypt

Enas Elmowafy – Department of Pharmaceutics and Industrial Pharmacy, Faculty of Pharmacy, Ain Shams University, Cairo, Egypt

Ahmed El-khouly – Department of Organic and Medicinal Chemistry, Faculty of Pharmacy, University of Sadat City, Sadat City, Egypt; Department of Pharmaceutical Sciences, Faculty of Pharmacy, Jerash University, Jerash, Jordan

Mai Mansour – Department of Pharmaceutics and Industrial Pharmacy, Faculty of Pharmacy, Ain Shams University, Cairo, Egypt

Gehanne A.S. Awad – Department of Pharmaceutics and Industrial Pharmacy, Faculty of Pharmacy, Ain Shams University, Cairo, Egypt

Complete contact information is available at: <https://pubs.acs.org/10.1021/acsomega.0c06046>

Author Contributions

Study design, data analysis, discussion, manuscript writing, and proofreading: M.H., H.M.A.-B., E.E., A.E.-K., M.M., and G.A.S.A. Experiments: M.H. and in silico molecular docking: A.E.-K. Supervision, manuscript review, and editing: H.M.A.-B., E.E., and G.A.S.A.

Notes

The authors declare no competing financial interest.

■ ACKNOWLEDGMENTS

The authors acknowledge the Faculty of Pharmacy, University of Sadat City, Egypt for providing the required facilities to conduct this study. Table of content and Scheme 1 were created with BioRender.com.

REFERENCES

- (1) Bhavana, V.; Thakor, P.; Singh, S. B.; Mehra, N. K. COVID-19: Pathophysiology, treatment options, nanotechnology approaches, and research agenda to combating the SARS-CoV2 pandemic. *Life Sci.* **2020**, *261*, No. 118336.
- (2) Zhou, P.; Yang, X.-L.; Wang, X.-G.; Hu, B.; Zhang, L.; Zhang, W.; Si, H.-R.; Zhu, Y.; Li, B.; Huang, C.-L.; Chen, H.-D.; Chen, J.; Luo, Y.; Guo, H.; Jiang, R.-D.; Liu, M.-Q.; Chen, Y.; Shen, X.-R.; Wang, X.; Zheng, X.-S.; Zhao, K.; Chen, Q.-J.; Deng, F.; Liu, L.-L.; Yan, B.; Zhan, F.-X.; Wang, Y.-Y.; Xiao, G.-F.; Shi, Z.-L. A pneumonia outbreak associated with a new coronavirus of probable bat origin. *Nature* **2020**, *579*, 270–273.
- (3) Hoffmann, M.; Kleine-Weber, H.; Schroeder, S.; Krüger, N.; Herrler, T.; Erichsen, S.; Schiergens, T. S.; Herrler, G.; Wu, N. H.; Nitsche, A.; Müller, M. A.; Drosten, C.; Pöhlmann, S. SARS-CoV-2 Cell Entry Depends on ACE2 and TMPRSS2 and Is Blocked by a Clinically Proven Protease Inhibitor. *Cell* **2020**, *181*, 271–280.e8.
- (4) V'Kovski, P.; Gerber, M.; Kelly, J.; Pfaender, S.; Ebert, N.; Braga Lagache, S.; Simillion, C.; Portmann, J.; Stalder, H.; Gaschen, V.; Bruggmann, R.; Stoffel, M. H.; Heller, M.; Dijkman, R.; Thiel, V. Determination of host proteins composing the microenvironment of coronavirus replicase complexes by proximity-labeling. *eLife* **2019**, *8*, e42037.
- (5) Gil, C.; Ginex, T.; Maestro, I.; Nozal, V.; Barrado-Gil, L.; Cuesta-Geijo, M. A.; Urquiza, J.; Ramírez, D.; Alonso, C.; Campillo, N. E.; Martínez, A. COVID-19: Drug Targets and Potential Treatments. *J. Med. Chem.* **2020**, No. 12359.
- (6) Jiang, J.; Pi, J.; Cai, J. The Advancing of Zinc Oxide Nanoparticles for Biomedical Applications. *Bioinorg. Chem. Appl.* **2018**, *2018*, No. 1062562.
- (7) Prasad, A. S. Zinc in human health: effect of zinc on immune cells. *Mol. Med.* **2008**, *14*, 353–357.
- (8) te Velthuis, A. J.; van den Worm, S. H.; Sims, A. C.; Baric, R. S.; Snijder, E. J.; van Hemert, M. J. Zn(2+) inhibits coronavirus and arterivirus RNA polymerase activity in vitro and zinc ionophores block the replication of these viruses in cell culture. *PLoS Pathog.* **2010**, *6*, No. e1001176.
- (9) Lanke, K.; Krenn, B. M.; Melchers, W. J.; Seipelt, J.; van Kuppeveld, F. J. PDTC inhibits picornavirus polyprotein processing and RNA replication by transporting zinc ions into cells. *J. Gen. Virol.* **2007**, *88*, 1206–1217.
- (10) Kumar, A.; Kubota, Y.; Chernov, M.; Kasuya, H. Potential role of zinc supplementation in prophylaxis and treatment of COVID-19. *Med. Hypotheses* **2020**, *144*, 109848–109848.
- (11) Tavakoli, A.; Ataei-Pirkooh, A.; Mm Sadeghi, G.; Bokharaei-Salim, F.; Sahrpour, P.; Kiani, S. J.; Moghooei, M.; Farahmand, M.; Javanmard, D.; Monavari, S. H. Polyethylene glycol-coated zinc oxide nanoparticle: an efficient nanoweapon to fight against herpes simplex virus type 1. *Nanomedicine (London, England)* **2018**, *13*, 2675–2690.
- (12) Maduray, K.; Parboosing, R. Metal Nanoparticles: a Promising Treatment for Viral and Arboviral Infections. *Biol. Trace Elem. Res.* **2020**, 1–18.
- (13) Aderibigbe, B. A. Metal-Based Nanoparticles for the Treatment of Infectious Diseases. *Molecules* **2017**, *22*, 1370.
- (14) Galdiero, S.; Falanga, A.; Vitiello, M.; Cantisani, M.; Marra, V.; Galdiero, M. Silver nanoparticles as potential antiviral agents. *Molecules* **2011**, *16*, 8894–8918.
- (15) Rai, M.; Deshmukh, S. D.; Ingle, A. P.; Gupta, I. R.; Galdiero, M.; Galdiero, S. Metal nanoparticles: The protective nanoshield against virus infection. *Crit. Rev. Microbiol.* **2016**, *42*, 46–56.
- (16) Ghaffari, H.; Tavakoli, A.; Moradi, A.; Tabarraei, A.; Bokharaei-Salim, F.; Zahmatkeshan, M.; Farahmand, M.; Javanmard, D.; Kiani, S. J.; Eshghaei, M.; Pirhajati-Mahabadi, V.; Monavari, S. H.; Ataei-Pirkooh, A. Inhibition of H1N1 influenza virus infection by zinc oxide nanoparticles: another emerging application of nanomedicine. *J. Biomed. Sci.* **2019**, *26*, 70.
- (17) Mishra, P. K.; Mishra, H.; Ekielski, A.; Talegaonkar, S.; Vaidya, B. Zinc oxide nanoparticles: a promising nanomaterial for biomedical applications. *Drug Discovery Today* **2017**, *22*, 1825–1834.
- (18) Xiong, H. M. ZnO nanoparticles applied to bioimaging and drug delivery. *Adv. Mater.* **2013**, *25*, 5329–5335.
- (19) Zhang, Z.-Y.; Xiong, H.-M. Photoluminescent ZnO Nanoparticles and Their Biological Applications. *Materials* **2015**, *8*, 3101–3127.
- (20) Ungula, J.; Dejene, B. F.; Swart, H. C. Effect of pH on the structural, optical and morphological properties of Ga-doped ZnO nanoparticles by reflux precipitation method. *Phys. B* **2018**, *535*, 251–257.
- (21) Hoshyar, N.; Gray, S.; Han, H.; Bao, G. The effect of nanoparticle size on in vivo pharmacokinetics and cellular interaction. *Nanomedicine (London, England)* **2016**, *11*, 673–692.
- (22) Agarwal, H.; Shanmugam, V. K. Synthesis and optimization of zinc oxide nanoparticles using *Kalanchoe pinnata* towards the evaluation of its anti-inflammatory activity. *J. Drug Delivery Sci. Technol.* **2019**, *54*, No. 101291.
- (23) Thirugnanam, T. Effect of Polymers (PEG and PVP) on Sol-Gel Synthesis of Microsized Zinc Oxide. *J. Nanomater.* **2013**, *2013*, No. 362175.
- (24) Edalati, K.; Shakiba, A.; Vahdati-Khaki, J.; Zebarjad, S. M. Low-temperature hydrothermal synthesis of ZnO nanorods: Effects of zinc salt concentration, various solvents and alkaline mineralizers. *Mater. Res. Bull.* **2016**, *74*, 374–379.
- (25) Kiomarsipour, N.; Shoja Razavi, R. Hydrothermal synthesis and optical property of scale- and spindle-like ZnO. *Ceram. Int.* **2013**, *39*, 813–818.
- (26) Wang, H.; Qiao, X.; Chen, J.; Ding, S. Preparation of silver nanoparticles by chemical reduction method. *Colloids Surf., A* **2005**, *256*, 111–115.
- (27) Khan, M. F.; Ansari, A. H.; Hameedullah, M.; Ahmad, E.; Husain, F. M.; Zia, Q.; Baig, U.; Zaheer, M. R.; Alam, M. M.; Khan, A. M.; AlOthman, Z. A.; Ahmad, I.; Ashraf, G. M.; Aliev, G. Sol-gel synthesis of thorn-like ZnO nanoparticles endorsing mechanical stirring effect and their antimicrobial activities: Potential role as nano-antibiotics. *Sci. Rep.* **2016**, *6*, 27689–27689.
- (28) Mahamuni, P. P.; Patil, P. M.; Dhanavade, M. J.; Badiger, M. V.; Shadjia, P. G.; Lokhande, A. C.; Bohara, R. A. Synthesis and characterization of zinc oxide nanoparticles by using polyol chemistry for their antimicrobial and antibiofilm activity. *Biochem. Biophys. Res.* **2019**, *17*, 71–80.
- (29) Jung, M.-H.; Chu, M.-J. Synthesis of hexagonal ZnO nanodrums, nanosheets and nanowires by the ionic effect during the growth of hexagonal ZnO crystals. *J. Mater. Chem. C* **2014**, *2*, 6675–6682.
- (30) Khoshhesab, Z. M.; Sarfaraz, M.; Asadabad, M. A. Preparation of ZnO Nanostructures by Chemical Precipitation Method. *Synth. React. Inorg. Met.-Org. Nano-Met. Chem.* **2011**, *41*, 814–819.
- (31) Kim, O.; Kwon, J.; Kim, S.; Xu, B.; Seo, K.; Park, C.; Do, W.; Bae, J.; Kang, S. Effect of PVP-Capped ZnO Nanoparticles with Enhanced Charge Transport on the Performance of P3HT/PCBM Polymer Solar Cells. *Polymer* **2019**, *11*, 1818.
- (32) Aboorvakani, R.; Kennady Vethanathan, S. J.; Madhu, K. U. Influence of Zn concentration on zinc oxide nanoparticles and their anti-corrosion property. *J. Alloys Compd.* **2020**, *834*, No. 155078.
- (33) Žūkienė, R.; Snitka, V. Zinc oxide nanoparticle and bovine serum albumin interaction and nanoparticles influence on cytotoxicity in vitro. *Colloids Surf., B* **2015**, *135*, 316–323.
- (34) Kim, K.-M.; Choi, M.-H.; Lee, J.-K.; Jeong, J.; Kim, Y.-R.; Kim, M.-K.; Paek, S.-M.; Oh, J.-M. Physicochemical properties of surface charge-modified ZnO nanoparticles with different particle sizes. *Int. J. Nanomed.* **2014**, *9 Suppl 2*, 41–56.
- (35) Taylor, Z.; Marucho, M. The Self-Adaptation Ability of Zinc Oxide Nanoparticles Enables Reliable Cancer Treatments. *Nanomaterials (Basel)* **2020**, *10*, 269.
- (36) Bian, S.-W.; Mudunkotuwa, I. A.; Rupasinghe, T.; Grassian, V. H. Aggregation and Dissolution of 4 nm ZnO Nanoparticles in Aqueous Environments: Influence of pH, Ionic Strength, Size, and Adsorption of Humic Acid. *Langmuir* **2011**, *27*, 6059–6068.
- (37) Buchegger, S.; Kamenac, A.; Fuchs, S.; Herrmann, R.; Houdek, P.; Gorzelanny, C.; Obermeier, A.; Heller, S.; Burgkart, R.; Stritzker, B.;

- Wixforth, A.; Westerhausen, C. Smart antimicrobial efficacy employing pH-sensitive ZnO-doped diamond-like carbon coatings. *Sci. Rep.* **2019**, *9*, 17246.
- (38) Xia, T.; Kovochich, M.; Liong, M.; Mädler, L.; Gilbert, B.; Shi, H.; Yeh, J. I.; Zink, J. I.; Nel, A. E. Comparison of the Mechanism of Toxicity of Zinc Oxide and Cerium Oxide Nanoparticles Based on Dissolution and Oxidative Stress Properties. *ACS Nano* **2008**, *2*, 2121–2134.
- (39) Chen, R.; Wang, S.; Zhang, J.; Chen, M.; Wang, Y. Aloe-emodin loaded solid lipid nanoparticles: formulation design and in vitro anti-cancer study. *Drug Delivery* **2015**, *22*, 666–674.
- (40) Abo-zeid, Y.; Ismail, N. S. M.; McLean, G. R.; Hamdy, N. M. A molecular docking study repurposes FDA approved iron oxide nanoparticles to treat and control COVID-19 infection. *Eur. J. Pharm. Sci.* **2020**, *153*, No. 105465.
- (41) Chouke, P. B.; Potbhare, A. K.; Dadure, K. M.; Mungole, A. J.; Meshram, N. P.; Chaudhary, R. R.; Rai, A. R.; Chaudhary, R. G. An antibacterial activity of Bauhinia racemosa assisted ZnO nanoparticles during lunar eclipse and docking assay. *Mater. Today: Proc.* **2020**, *29*, 815–821.
- (42) Prasad, A. R.; Basheer, S. M.; Williams, L.; Joseph, A. Highly selective inhibition of α -glucosidase by green synthesised ZnO nanoparticles - In-vitro screening and in-silico docking studies. *Int. J. Biol. Macromol.* **2019**, *139*, 712–718.
- (43) Patil, R.; Das, S.; Stanley, A.; Yadav, L.; Sudhakar, A.; Varma, A. K. Optimized hydrophobic interactions and hydrogen bonding at the target-ligand interface leads the pathways of drug-designing. *PLoS One* **2010**, *5*, e12029–e12029.
- (44) Chen, D.; Oezguen, N.; Urvil, P.; Ferguson, C.; Dann, S. M.; Savidge, T. C. Regulation of protein-ligand binding affinity by hydrogen bond pairing. *Sci. Adv.* **2016**, *2*, No. e1501240.
- (45) Pansar, T.; Poso, A. Binding Affinity via Docking: Fact and Fiction. *Molecules* **2018**, *23*, 1899.
- (46) Overbeck, S.; Rink, L.; Haase, H. Modulating the immune response by oral zinc supplementation: a single approach for multiple diseases. *Arch. Immunol. Ther. Exp.* **2008**, *56*, 15–30.
- (47) Wessels, I.; Rolles, B.; Rink, L. The Potential Impact of Zinc Supplementation on COVID-19 Pathogenesis. *Front. Immunol.* **2020**, *11*, 1712.
- (48) Roscioli, E.; Jersmann, H. P.; Lester, S.; Badiel, A.; Fon, A.; Zalewski, P.; Hodge, S. Zinc deficiency as a codeterminant for airway epithelial barrier dysfunction in an ex vivo model of COPD. *Int. J. Chronic Obstruct. Pulm. Dis.* **2017**, *12*, 3503–3510.
- (49) Wessels, I.; Pupke, J. T.; von Trotha, K. T.; Gombert, A.; Himmelsbach, A.; Fischer, H. J.; Jacobs, M. J.; Rink, L.; Grommes, J. Zinc supplementation ameliorates lung injury by reducing neutrophil recruitment and activity. *Thorax* **2020**, *75*, 253–261.
- (50) Christianson, D. W.; Alexander, R. S. Carboxylate-histidine-zinc interactions in protein structure and function. *J. Am. Chem. Soc.* **1989**, *111*, 6412–6419.
- (51) Cox, E. H.; McLendon, G. L. Zinc-dependent protein folding. *Curr. Opin. Chem. Biol.* **2000**, *4*, 162–165.
- (52) Denison, M. R.; Zoltick, P. W.; Hughes, S. A.; Giangreco, B.; Olson, A. L.; Perlman, S.; Leibowitz, J. L.; Weiss, S. R. Intracellular processing of the N-terminal ORF 1a proteins of the coronavirus MHV-A59 requires multiple proteolytic events. *Virology* **1992**, *189*, 274–284.
- (53) Liu, C. Y.; Kielian, M. Identification of a specific region in the e1 fusion protein involved in zinc inhibition of semliki forest virus fusion. *J. Virol.* **2012**, *86*, 3588–3594.
- (54) S, M.; N, H.; P.P, V. In Vitro Biocompatibility and Antimicrobial activities of Zinc Oxide Nanoparticles (ZnO NPs) Prepared by Chemical and Green Synthetic Route— A Comparative Study. *BioNanoScience* **2020**, *10*, 112–121.
- (55) Ishak, R. A. H.; Mostafa, N. M.; Kamel, A. O. Stealth lipid polymer hybrid nanoparticles loaded with rutin for effective brain delivery – comparative study with the gold standard (Tween 80): optimization, characterization and biodistribution. *Drug Delivery* **2017**, *24*, 1874–1890.
- (56) Wiesmann, N.; Tremel, W.; Brieger, J. Zinc oxide nanoparticles for therapeutic purposes in cancer medicine. *J. Mater. Chem. B* **2020**, *8*, 4973–4989.
- (57) Kumar, A.; Pandey, A. K.; Singh, S. S.; Shanker, R.; Dhawan, A. A flow cytometric method to assess nanoparticle uptake in bacteria. *Cytometry. Part A* **2011**, *79*, 707–712.
- (58) Hong, H.; Shi, J.; Yang, Y.; Zhang, Y.; Engle, J. W.; Nickles, R. J.; Wang, X.; Cai, W. Cancer-Targeted Optical Imaging with Fluorescent Zinc Oxide Nanowires. *Nano Lett.* **2011**, *11*, 3744–3750.
- (59) Hamdi, M.; Abdel-Bar, H. M.; Elmowafy, E.; Al-Jamal, K. T.; Awad, G. A. S. An integrated vitamin E-coated polymer hybrid nanoplatfrom: A lucrative option for an enhanced in vitro macrophage retention for an anti-hepatitis B therapeutic prospect. *PLoS One* **2020**, *15*, No. e0227231.
- (60) Dumontel, B.; Canta, M.; Engelke, H.; Chiodoni, A.; Racca, L.; Ancona, A.; Limongi, T.; Canavese, G.; Cauda, V. Enhanced biostability and cellular uptake of zinc oxide nanocrystals shielded with a phospholipid bilayer. *J. Mater. Chem. B* **2017**, *5*, 8799–8813.
- (61) Djearmane, S.; Lim, Y. M.; Wong, L. S.; Lee, P. F. Cellular accumulation and cytotoxic effects of zinc oxide nanoparticles in microalga *Haematococcus pluvialis*. *PeerJ* **2019**, *7*, No. e7582. PubMed. <http://europepmc.org/abstract/MED/31579572>, <https://europepmc.org/articles/PMC6765357>, <https://europepmc.org/articles/PMC6765357?pdf=render> (accessed 2019).
- (62) Devi, P. G.; Velu, A. S. Synthesis, structural and optical properties of pure ZnO and Co doped ZnO nanoparticles prepared by the co-precipitation method. *J. Theor. Appl. Phys.* **2016**, *10*, 233–240.
- (63) Kim, S.; Lee, S. Y.; Cho, H. J. Doxorubicin-Wrapped Zinc Oxide Nanoclusters for the Therapy of Colorectal Adenocarcinoma. *Nanomaterials (Basel)* **2017**, *7*, 354.
- (64) Tada-Oikawa, S.; Ichihara, G.; Suzuki, Y.; Izuoka, K.; Wu, W.; Yamada, Y.; Mishima, T.; Ichihara, S. Zn(II) released from zinc oxide nano/micro particles suppresses vasculogenesis in human endothelial colony-forming cells. *Toxicol. Rep.* **2015**, *2*, 692–701.
- (65) Anupama, R.; Lulu, S.; Madhusmita, R.; Vino, S.; Mukherjee, A.; Babu, S. Insights into the interaction of key biofilm proteins in *Pseudomonas aeruginosa* PAO1 with TiO₂ nanoparticle: An in silico analysis. *J. Theor. Biol.* **2019**, *462*, 12–25.
- (66) Momma, K.; Izumi, F. VESTA 3 for three-dimensional visualization of crystal, volumetric and morphology data. *J. Appl. Crystallogr.* **2011**, *44*, 1272–1276.
- (67) Giannousi, K.; Geromichalos, G.; Kakolyri, D.; Mourdikoudis, S.; Dendrinou-Samara, C. Interaction of ZnO Nanostructures with Proteins: In Vitro Fibrillation/Antifibrillation Studies and in Silico Molecular Docking Simulations. *ACS Chem. Neurosci.* **2020**, *11*, 436–444.
- (68) Shityakov, S.; Broscheit, J.; Förster, C. α -Cyclodextrin dimer complexes of dopamine and levodopa derivatives to assess drug delivery to the central nervous system: ADME and molecular docking studies. *Int. J. Nanomed.* **2012**, *7*, 3211–3219.
- (69) Joshi, S. A.; Chavhan, S. S.; Sawant, K. K. Rivastigmine-loaded PLGA and PBCA nanoparticles: preparation, optimization, characterization, in vitro and pharmacodynamic studies. *Eur. J. Pharm. Biopharm.* **2010**, *76*, 189–199.
- (70) Patel, P.; Kansara, K.; Senapati, V. A.; Shanker, R.; Dhawan, A.; Kumar, A. Cell cycle dependent cellular uptake of zinc oxide nanoparticles in human epidermal cells. *Mutagenesis* **2016**, *31*, 481–490.